Chapter 2
Dental Tools, Human Tooth and Environment

Abstract The construction of dental burs and hand pieces are described in this chapter of the book. Initially, the chapter describes the characteristics of the bur focusing on design and the effect of different rake angles on cutting, then the chapter focuses on the design and construction of elements of the hand piece itself. The finals aspect explains the direction of research that needs to be taken in order to develop a hand piece that has been optimized for use with different dental materials.

Keywords Dental burs · Dental hand piece · Air turbine · Mechanical design · Fluid dynamics · Human tooth

2.1 Introduction

Dental burs are used for cutting hard tissues such as bone or tooth (O'Brien 1997). They are usually made of stainless steel, diamond grit or particles and tungsten carbide. Burs are rotary drill bits of various shapes and dimensions used by the dentist in his dental drill incorporating an air turbine. The development of the dental bur dates back approximately 300 years. The drill bit for dental work has revolutionised the field of dentistry.

A dental bur consists of three parts, which include bur head, bur neck and shank. The bur head contains the blades that rotate at high speed to cut and remove material from the teeth (Sein et al. 2002). They can be positioned at various angles to remove unwanted material such as plaque from difficult to get at areas. The positive rake angle, which is also called the acute angle, has a sharper blade, which dulls rapidly during use. The obtuse angle produce negative rake angle, which makes the bur stronger and last longer. Dental technicians also use burs to prepare dental materials in the laboratory.

In order to appreciate the role dental burs are playing in dentistry it is informative here to give some background into the oral environment. Normally an adult

W. Ahmed et al., *Chemical Vapour Deposition of Diamond for Dental Tools and Burs*, SpringerBriefs in Materials, DOI: 10.1007/978-3-319-00648-2_2,

human has 32 teeth, which are aligned in two dental arches. First one is called maxillary arches, and the second is called madibular arches. A single tooth consists of a crown with neck, one or more cusps, and a root (Seely et al. 2007). The clinical crown is the part of the tooth exposed in the oral cavity, and is entirely enamel. The pulp cavity is filled with nerves, blood vessels, and connecting tissue. Root canal is situated in the pulp cavity within the root. The nerves and blood vessels of the tooth have inlet and outlet routes to the pulp through a hole at the point of each root. It is commonly called epical foramen. The pulp cavity is surrounded by living, cellular, calcified tissue called dentine. The dentine of the crown is covered by non-living, acellular substance called enamel, which is very hard and protects the tooth against abrasion and acid produced from bacteria in the mouth. When the tooth becomes weaker and soft tissues break down and can cause pain. Untreated cavities cause diseases such as dental caries and abscesses requiring treatment by a qualified dentist (Seely et al. 2007).

The modern day dental bur has the ability to allow dentists to work more efficiently and accurately with less pain. The future goal of dentistry is to maintain and improve the dental health of patients. This can be achieved in a number of ways such as disease prevention, improved mastication efficiency, and relieves pain, speech and appearance. These objectives can be achieved by employing better dental tools that are durable, long lasting, biocompatible, and cost effective.

A major aim of this research project is to evaluate the performance of CVD diamond coated dental burs and micro drill cutting tools within simulated clinical and laboratory conditions. The goal for these surface engineered cutting tools is to improve the product quality, cutting performance and life expectancy (Sein et al. 2002; Ahmed et al. 2004).

2.2 Dental Burs

A dental bur or dentist's drill is used to remove decayed tooth material before applying a filling. Dental burs may come in various shapes and sizes designed for specific applications and can rotate up to 500,000 rpm. Steel is a widely used material for making burs, coated with a hard WC coating. They can also be entirely made by sintered WC (Trava-Airoldi et al. 1996a, b; Carvalho et al. 2007). In recent years the bur has been diamond coated using CVD (Trava-Airoldi et al. 1996a, b). There are numerous shapes of burs manufactured for varying applications, cutting and drilling abilities.

2.2.1 Dental Bur Construction and Geometry

Each dental bur comprises of three main parts; shank, shaft and bur head (the cutting edge). Since the bur is composed of a single parent material (with the

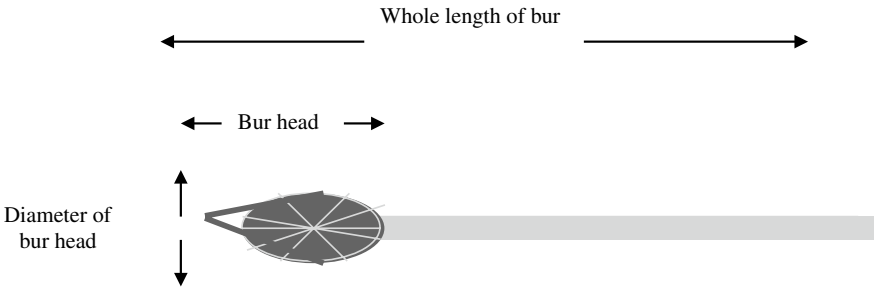

Fig. 2.1 Schematic of the various parts of a dental bur

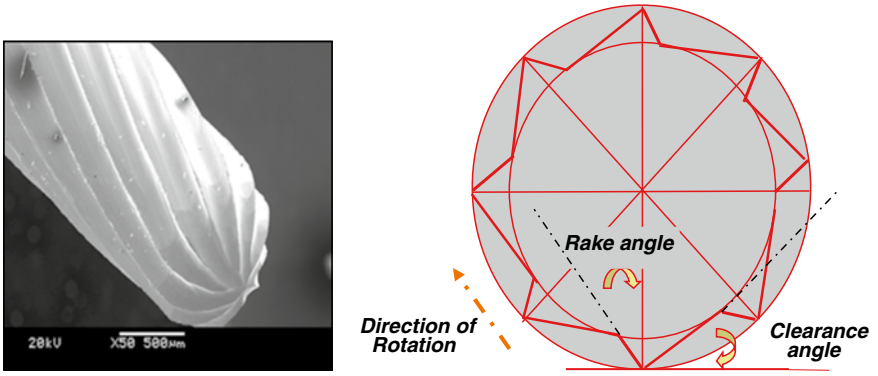

Fig. 2.2 Geometry of a typical tungsten carbide bur and schematic diagram showing the rake angle relative to the cutting direction (Sein et al. 2004a, b)

possibility of a coating along the cutting surfaces) the choice of this material is important (see Fig. 2.1). It must provide a good cutting edge, but also be able to withstand the forces endured by the shaft throughout the cutting process.

The basic design of an eight bladed fissure bur is indicated in Fig. 2.2. Most burs have a negative rake angle. Those with a positive rake angle are designed mainly for cutting soft materials (e.g. acrylics). This is designed to remove material during cutting to prevent the tool from clogging with cut material or chips.

When the rake angle of a bur blade is too steep, subsurface damage occurs in the tooth. These weak areas become sites for later bacterial infection. When the rake angle is decreased, a more gentle action is achieved and less residual subsurface damage occurs to the tooth but life of the bur is decreased due to the acute angle of the cutting tips. The rake angles come in two different varieties positive and negative (Fig. 2.3).

If the leading edge of the blade is behind the perpendicular the angle is by definition positive. Examples of positive angle instruments are finecut files, hedstrom files and most dental burs when run normally.

If leading the edge of blade is ahead of perpendicular, the angle is by definition, negative. Examples of negative angle instruments are reamers and diamond burs

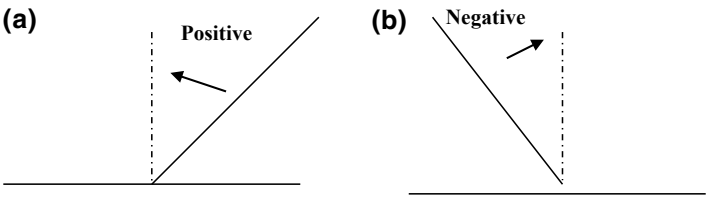

Fig. 2.3 **a** Positive rake angle, **b** negative rake angle

and burnishing burs when runs backward. The geometrical design features also impact on the performance and wear rates (Polini et al. 2004).

2.3 Bur Materials

The two most common dental bur materials used are stainless steal and tungsten carbide.

2.3.1 Stainless Steel Bur

Steel wears rapidly and corrodes easily. This does not make it appear to be a good choice for burs. However, limiting the use of steel burs to lower speeds significantly reduces the wear rate associated with the cutting process. The main corrosive environment experienced by a bur is during the sterilisation process, although the conditions in the oral cavity will also contribute (Dietz et al. 2000). Stainless steel provides a less efficient cutting edge than carbon steel, but is more corrosion resistant. Stainless steel is also a cheap material, which makes it suitable for burs provided that they are considered single-use and classed as disposable burs.

2.3.2 Tungsten Carbide WC-Co Bur

Tungsten carbide is an extremely hard material, which makes it suitable for use at very high speeds. Unfortunately, associated with the additional hardness of WC, relative to stainless steel, is an increase in brittleness. Therefore only the blades of a bur should be made of tungsten carbide (the shank being made of steel). Sintering the carbide blades onto the steel shank joins the two components. Tungsten carbide is also suitable for burs designated for use at lower speeds, when they are to be used many times. Instruments made from tungsten carbide are much more expensive than their steel equivalents, but compensate for this by their increased working life (Sein et al. 2003). WC burs contains cobalt as a binder, which provides additional toughness to the tool. Most WC-Co dental burs contain about 6 % Co as a binder material. There are two parameters of importance these

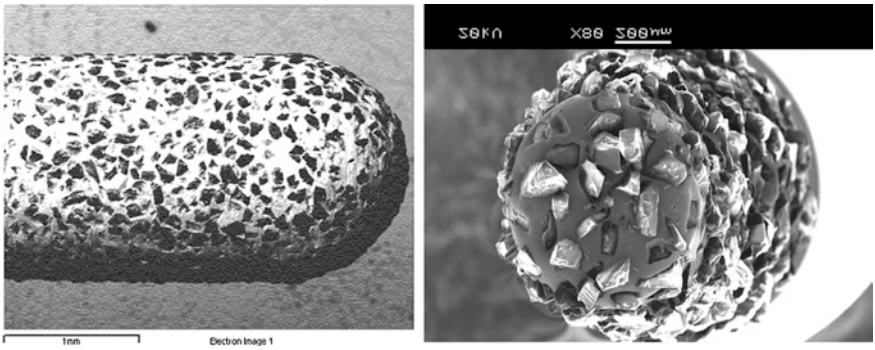

Fig. 2.4 SEM of a conventional sintered diamond bur showing lateral and *top views* (Sein et al. 2004a, b)

are the Co/WC ratio and the WC particle size. These parameters have a significant impact on the control of the bulk material properties (Jian et al. 2004). In general, course grained WC combined with a high % Co give better shock resistance and impact strength. However, finer grained WC and thus larger surface area and lower % Co gives harder and greater wear resistance (Jian et al. 2004).

Therefore to achieve optimum performance premature failure needs to be avoided whilst at the same time achieving a higher wears resistance (Yared et al. 2001).

2.3.3 Sintered Polycrystalline Diamond Dental Bur

As discussed in the previous section the diamond bur is a favoured instrument of both dentists and dental technicians (Sein et al. 2004a, b, 2006). Since the 1950s conventional diamond bur technology uses small diamond particles bonded onto the substrate using a binder matrix material (Fig. 2.4); its use is however limited due to variation in the grain sizes and grain shapes, problems in the automation of the fabrication process and the short tool life. Sterilisation of the instruments also decreases the cutting effectiveness and results in diamond particle loss causing oral contamination (Siegel and von Fraunhofer 1999).

2.4 Operation Conditions

Many different designs of dentals trepan are available in the marketplace. They must however have common features (see Fig. 2.5). These include the following:

- Drill bit
- Motor
- Couplings
- Hand piece

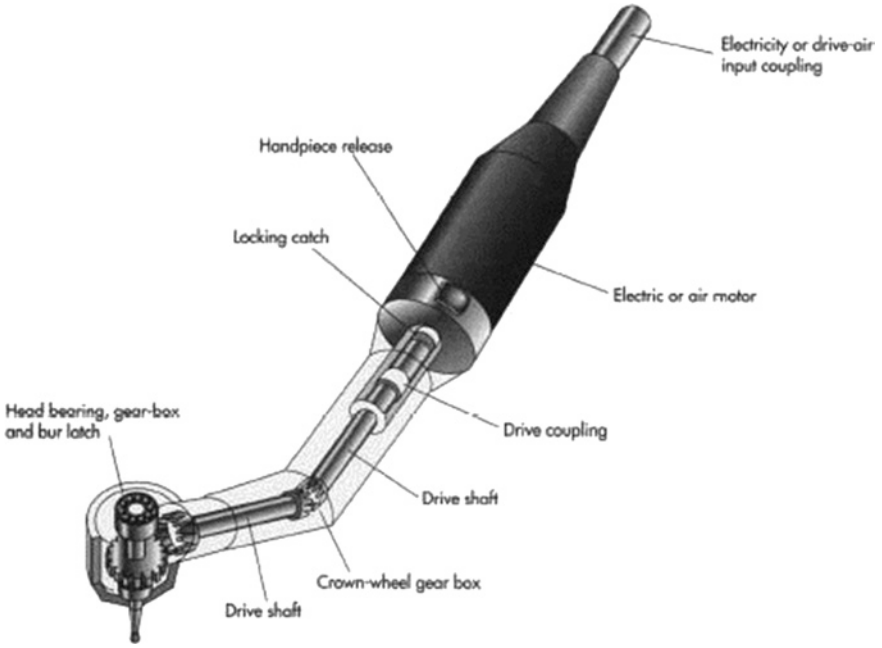

Fig. 2.5 High speed dental handpiece. http://www.gs-dental.com/UpFile/2009313114114.jpg

An air turbine activates the high speed drilling up to 0.5 million rpm. Many operations require slower speeds and therefore dental drills also have secondary motors. For example, polishing, finishing, and soft tissue drilling require the slower rotational speeds. Electric motors and air-driven motors are widely used.

The hand piece is a well-designed, slender and lightweight tube-shaped device. This connects the drill bit and a motor that provides the driving force during its use. During the early phases of their developments, dental drill components were somewhat delicate. However, health risks and legislation has forced changes in the way in which the dentil drill is designed. The hand piece can now withstand high-pressure steam sterilization. The drill bit or bur is a highly important component and needs to be robust, durable and be able to rotate at very high speeds. These high speeds generate a lot of heat, which needs to be removed using water-cooling. Modern devices have addition features such as illumination devices to aid the dentist in performing cutting, drilling and grinding operations.

Each bur is designed to operate at an optimum speed and intended for use in a specific hand piece motor combination. The optimum speed is also dependent upon the nature of the material being cut. Cutting speed can be separated into two categories each using different burs and designed for different types of operations.

2.4.1 Low Speed Hand Piece

A miniature compressed air or electric motor is used to drive low speed hand pieces. They operated with rotational speeds of up to 4,000 rpm. The burs used in low speed operations are used to trim dentures and remove decayed tissue. These burs may be made of stainless steel.

2.4.2 High-Speed Hand Piece

Air turbine hand piece can run up to 500,000 rpm, although they are rarely used at such high speeds. General operating speeds are approximately 20,000–50,000 rpm (varying with the diameter of the bur). The burs used at high speeds are mainly diamond-coated or made of tungsten carbide. High speeds are used in the removal of enamel, dentine and old fillings. When operating at such high speeds, a built in water spray is used as a coolant, protecting both the bur and tooth. The efficiency of micro cutting tools that are used in high-speed air turbine spindles depends on the rotational speed of the rotor. A high-pressure variation on the surface of the rotor causes the rotor to retard and this severely limits the reliability and durability of high-speed spindles. A variety of spindle designs are proposed and numerical simulations carried out for each design using CFD FLUENT^{TM} simulation software. The results revealed that changes in the rotor, inlet, and outlet geometries affect the pressure distribution on the rotor significantly. The optimum design was identified based on the lowest pressure variation on the rotor surface obtained from the FLUENT^{TM} results. Spinning the rotor at very high speeds provides a new direction in the development of dental cutting tools.

The major components of a high-speed air turbine spindle are: bearings, rotor, stator, and spindle shaft. To drive a high-speed spindle a motor, or compressor, is integrated with the spindle shaft. Bearings provide stability at high speeds to prevent chatter and poor surface finish and to permit accurate cutting tool paths. The speed of the spindle depends on the rotational speed of the rotor. The spindle shaft, rotor, and bearings must be held in the housing. High-pressure compressed air enters into the housing of the spindle from the compressor through a pneumatic connector. The compressed air enters the housing through the shaft and rotates the rotor of the spindle. The micro cutting tool, which is attached to the centre of the rotor, rotates with the speed of the rotor and cuts the workpiece more quickly than conventional spindles. The rotor is supported by an air bearing, which provides stability to the rotor and also transmits the necessary torque.

In high speed machining with high-speed spindles, the pressure variation on the rotor surface is of vital importance. The pressure coefficient is defined as the difference between the highest and lowest pressure on the rotor surface, normalized by the imposed inlet pressure. Pressure coefficient determines pressure variation exerted by high-speed compressed air on the rotor and for the optimum design of the rotor, the pressure coefficient should be as low as possible as the large values of pressure

coefficient indicate high pressure variations, which could cause the severe imbalance of the load and deformation of the rotor and this generates failure of the rotor. Various designs of rotor for different rotational speeds are proposed and fluid analysis of rotors has been carried out with a computational fluid dynamics (CFD) software package called FLUENT^{TM}. Pressure coefficients of rotors were calculated and compared for different designs of rotor to determine the optimum design of the rotor.

2.4.2.1 Analysis of Fluid Flow

1. Assumptions
   The following assumptions were considered for the numerical solution of high-speed spindles (HSS) using computational fluid dynamics (CFD):

- HSS rotor rotational speed depends on the pressure of the compressed air entering from the compressor. The numerical simulation was carried out by a considering de-coupled system, i.e., for a given inlet pressure (60 psi), the rotating speed of the rotor was assumed as a constant value such as half-million rpm, i.e., the current study deals only with the fluid problem, not the fluid/structure problem;
- Steady-state simulation was assumed for all numerical simulations.

2. CFD Geometry Model
   The bearing component of the HSS was omitted in the CFD model. The outer diameter of the rotor is 0.3 inches (7.6 mm), inner diameter of the rotor is 0.092 inches (2.34 mm), the height along the z-direction is 0.1445 inches (3.6 mm) and the angle between the rotor blades is 90°. A cylindrical housing with a diameter of 0.31 inches (7.8 mm) was modelled around the rotor with a height of 0.1735 inches (4.4 mm) so that the rotor could rotate freely inside the housing. The spindle is driven by compressed air. Three inlets, with a diameter of 0.055 inches (1.4 mm), that make an angle of 120° with each other, were created around the housing. The inlets were created at an angle of 45°. An outlet for the air was created at the centre of the housing.

3. Fluid Model
   The air was considered as an ideal gas. The flow in HSS is turbulent. The turbulence is described by k-ε turbulent model, in which k is the turbulence kinetic energy and ε is the turbulence eddy dissipation. The total energy heat transfer model was considered as kinetic energy effects are important in the model.

Applied Boundary Conditions

The following boundary conditions were applied to the model:

- Static pressure of 60 psi at the inlets;
- Static pressure of 0 (zero) at the outlet;
- A no-slip (moving) wall boundary condition on the rotor. A constant angular speed of the rotor was specified;
- A no-slip (stationary) wall boundary condition on the housing and inlet surfaces.

Governing Equations

The governing equations of three-dimensional fluid flow were represented as:
Continuity Equation:

$$\frac{\partial(\rho U_i)}{\partial X_i} = 0 \tag{2.1}$$

Momentum Equation:

$$\frac{\partial\left(\rho \mathrm{U_i U_j}\right)}{\partial \mathrm{x_j}} = -\frac{\partial \mathrm{P}}{\partial \mathrm{x_i}} + \frac{\partial}{\partial \mathrm{x_j}}\left(\mu_{\mathrm{eff}}\frac{\partial \mathrm{U_i}}{\partial \mathrm{x_j}} + \mu_{\mathrm{eff}}\frac{\partial \mathrm{U_j}}{\partial \mathrm{x_i}}\right) \tag{2.2}$$

where repeated indices imply summation from 1 to 3, ρ is density, $\mathrm{U_i}$ are the cartesian velocity components, P is pressure, $\mathrm{X_i}$ are the coordinate axes, and μ_{eff} is the effective viscosity, which is defined as:

$$\mu_{eff} = \mu + \mu_t; \quad \mu_{\mathrm{t}} = \mathrm{C}_\mu \rho \frac{\mathrm{k}^2}{\varepsilon} \tag{2.3}$$

where μ_{t} is the eddy viscosity, C_μ is a constant and is equal to 0.09, k is the turbulence kinetic energy and ε is the turbulence eddy dissipation. The turbulence model is given by:

$$\begin{aligned}\frac{\partial \rho \mathrm{k}}{\partial \mathrm{t}} + \frac{\partial}{\partial \mathrm{x_j}}\left(\rho \mathrm{U_j k}\right) - \frac{\partial}{\partial \mathrm{x_j}}\left(\frac{\mu_{\mathrm{eff}}}{\sigma_{\mathrm{k}}}\frac{\partial \mathrm{k}}{\partial \mathrm{x_j}}\right) &= \mu_{\mathrm{t}}\frac{\partial \mathrm{U_i}}{\partial \mathrm{x_j}}\left(\frac{\partial \mathrm{U_i}}{\partial \mathrm{x_j}} + \frac{\partial \mathrm{U_j}}{\partial \mathrm{x_i}}\right) \\ &\quad - \frac{2}{3}\frac{\partial \mathrm{U_j}}{\partial \mathrm{x_j}}\left(\mu_{\mathrm{t}}\frac{\partial \mathrm{U_j}}{\partial \mathrm{x_j}} + \rho \mathrm{k}\right) - \rho\varepsilon\end{aligned} \tag{2.4}$$

and

$$\begin{aligned}\frac{\partial \rho \varepsilon}{\partial \mathrm{t}} + \frac{\partial}{\partial \mathrm{x_j}}\left(\rho \mathrm{U_j}\varepsilon\right) - \frac{\partial}{\partial \mathrm{x_j}}\left(\frac{\mu_{\mathrm{eff}}}{\sigma_\varepsilon}\frac{\partial \varepsilon}{\partial \mathrm{x_j}}\right) &= \frac{\varepsilon}{\mathrm{k}}\left(\mathrm{C}_{\varepsilon 1}\left(\mu_{\mathrm{t}}\frac{\partial \mathrm{U_i}}{\partial \mathrm{x_j}}\left(\frac{\partial \mathrm{U_i}}{\partial \mathrm{x_j}} + \frac{\partial \mathrm{U_j}}{\partial \mathrm{x_i}}\right)\right.\right. \\ &\quad \left.\left. - \frac{2}{3}\frac{\partial \mathrm{U_j}}{\partial \mathrm{x_j}}\left(\mu_{\mathrm{t}}\frac{\partial \mathrm{U_j}}{\partial \mathrm{x_j}} + \rho \mathrm{k}\right)\right) - \mathrm{C}_{\varepsilon 2}\rho\varepsilon\right)\end{aligned} \tag{2.5}$$

where σ_{k} and σ_ε are k-ε turbulence model constants and are equal to 1.0 and 1.3 respectively, and $\mathrm{C}_{\varepsilon 1}$ and $\mathrm{C}_{\varepsilon 2}$ are equal to 1.45 and 1.92, respectively:

Energy Equation:

$$\frac{\partial\left(\rho U_j h_{tot}\right)}{\partial X_j} = \frac{\partial\left(\lambda \frac{\partial T}{\partial X_j}\right)}{\partial X_j} + S_E \tag{2.6}$$

where $\mathrm{h_{tot}}$ is defined as the specific total enthalpy, which for the general case of variable properties is given in terms of the specific static enthalpy, h, by:

$$h_{tot} = h + \frac{1}{2}U^2; \quad h = h(p, T) \tag{2.7}$$

and S_E is the source term, which represents the work done by the viscous and pressure forces. The equation of state for an ideal gas is given as:

$$p = \rho RT \tag{2.8}$$

where T is the temperature of the fluid and R is the gas constant.

Pressure Coefficient

The parameter "pressure coefficient" was defined to determine the pressure variation on the rotor,

$$\text{Pressure coefficient} = \frac{P_{max} - P_{min}}{P_{inlet}} \tag{2.9}$$

where P_{max} = Maximum pressure exerted by air on the rotor, P_{min} = Minimum pressure exerted by air on the rotor, P_{inlet} = Air pressure at the inlet. Maximum pressure and minimum pressure exerted by air can be obtained by FLUENT™. Inlet pressure was used to non-dimensionalize the value of the pressure coefficient.

2.4.2.2 Experimental Results and Discussions

Flow topology and pressure variation of rotor geometries such as rotor with 90° blade angle, rotor with inlets, inclined at 45° to the z-axis of the rotor, and two-stage rotor are described and pressure coefficient values for all geometries are calculated. The optimum design of the high-speed spindle is identified based on the magnitude of the pressure coefficient.

Numerical Results

Numerical simulations of the spindle geometries were carried out using FLUENT™. Air was the ideal gas with an inlet pressure of 60 psi and an outlet pressure of zero, and the rotor was considered to be at no-slip conditions at the wall with specific rotational speeds such as half-million rpm, one million rpm, etc. The total number of control volumes for the numerical grid was approximately between 437,000 and 532,000 based on the geometry of the rotor, and the number of iterations for numerical simulations was 200. The maximum continuity loops are advantageous for achieving convergence especially for high-speed flows and the value of maximum continuity loops was specified as 2 for numerical simulations of all geometries under consideration. The governing equations such as continuity equation, momentum equation, energy equation, and equation of state were solved by FLUENT™ to provide the pressure distribution on the rotor. The pressure values were obtained using FLUENT™ and the pressure coefficient values were calculated using Eq. (2.9).

Initially, numerical simulations of rotor geometries such as the basic geometry of the rotor, rotor with fillets, rotor with 70° blade angle, and the rotor with

Table 2.1 Pressure coefficient values for rotor geometries such as basic geometry of the rotor, rotor with fillets, rotor with 70° blade angle and rotor with 90° blade angle for different rotational speeds

Rotational speed (RPM)	Basic geometry of rotor	Rotor with fillets	Rotor with 70° blade angle	Rotor with 90° blade angle
Half-million	0.11	0.10	0.09	0.07
One million	0.18	0.20	0.16	0.11
Two million	0.45	0.46	0.40	0.42
Five-Million	1.28	1.18	1.15	1.19

90° blade angle were carried out for different rotational speeds of the rotor such as half-million rpm, one million rpm, two million rpm, and five million rpm. The number of control volumes considered for the numerical simulation of basic geometry of the rotor was 437,273; for the numerical simulation of rotor with fillets it was 439,092; for the numerical simulation of rotor with 70° blade angle it was 488,786 and for the numerical simulation of rotor with 90° blade angle it was 520,324. The residual target for the convergence criterion was specified as 1e-6 and the maximum number of iterations considered for convergence control was 200 for the described geometries. The values of the non-dimensional pressure coefficients obtained form the numerical simulations are shown in Table 2.1 and displayed in Fig. 2.6.

From Table 2.1 it is observed that for a particular geometry as the rotating speed of the rotor increases, the pressure coefficient value increases because of the variation of pressure values on the surface of the rotor. Figure 2.7 shows the variation of pressure coefficient for the specified geometries with the rotational speeds of the rotor. From Table 2.1 it can be said that the pressure coefficient values of rotor with 90° blade angle are less than those of the other geometries of the rotor for the rotational speeds of half-million, one-million, and two-million rpm of the rotor which is in the typical range of micromachining operations. For two million and five million rpm rotational speed of rotor, the rotor with a 70° blade angle possessed pressure coefficient values that were less when compared to other geometries of the rotor. The geometry of the rotor with 90° blade angle was considered to be the optimum design compared to other geometries of the rotor for the rotational speeds that are in the typical range of micromachining conditions. Modifications in the spindle geometry were conducted by changing the number of blades of the rotor, changing the angle of the inlets, and by changing the number of inlets and outlets for the fluid. Numerical simulations of the rotor with twelve blades, rotor with three inlets inclined at an angle of 30°, rotor with three inlets inclined at an angle of 45°, and rotor with three inlets and three outlets were carried out. The number of control volumes associated with the numerical simulation of rotor with twelve blades it was 467,311; with that of rotor with three inlets inclined at an angle of 30° it was 513,116; with that of rotor with three inlets inclined at an angle of 45° it was 532,447 and with that of rotor with three inlets and three outlets it was 509,288. The residual target for satisfying the convergence criterion was

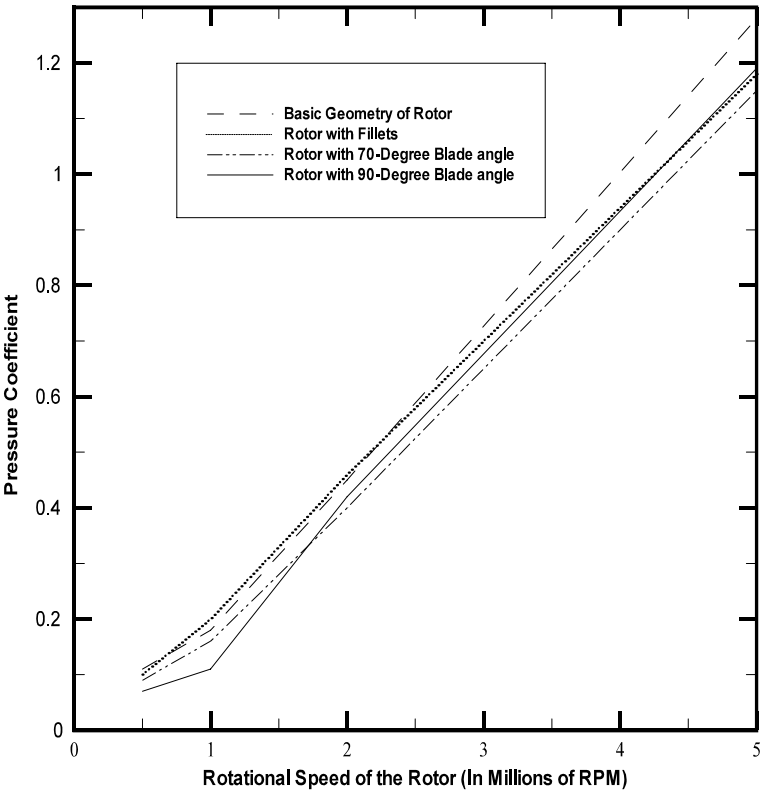

Fig. 2.6 Variation of pressure coefficient with rotating speed of the rotor for different geometries of the rotor such as basic geometry of the rotor, rotor with fillets, rotor with 70° blade angle and rotor with 90° blade angle. Reproduced with permission. Copyright retained by Inderscience Publishers

Table 2.2 Pressure coefficient values for rotor geometries of rotor with twelve blades, rotor with three inlets inclined at an angle of 30°, rotor with three inlets inclined at an angle of 45° and rotor with three inlets and three outlets

Rotational speed (RPM)	Rotor with twelve blades	Rotor with three inclined inlets at 30°	Rotor with three inclined inlets at 45°	Rotor with three inlets and three outlets
Half-million	0.09	0.10	0.08	0.36
One million	0.15	0.15	0.10	0.48
Two million	0.39	0.41	0.40	0.44
Five million	1.07	1.14	1.12	1.15

Reproduced with permission. Copyright retained by Inderscience Publishers

specified as 1e-6 and the maximum number of iterations specified for convergence control was 200. The pressure coefficient values obtained for these geometries for different rotational speeds of the rotor are shown in Table 2.2.

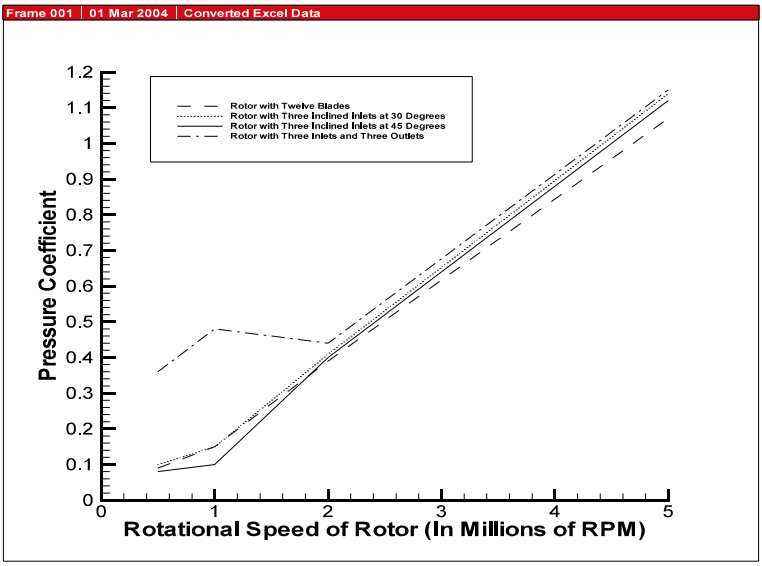

Fig. 2.7 Variation of pressure coefficient with rotating speed of the rotor for different geometries of the rotor such as rotor with twelve blades, rotor with three inlets inclined at an angle of 30°, rotor with three inlets inclined at an angle of 45°, and rotor with three inlets and three outlets. Reproduced with permission. Copyright retained by Inderscience Publishers

Figure 2.7 shows the variation of pressure coefficient values for rotor with twelve blades, rotor with inlets, inclined at an angle of 30°, rotor with inlets, inclined at an angle of 45° and rotor with three inlets and three outlets for different rotating speeds of the rotor. From Fig. 2.7 it could be said that as the rotating speed of the rotor increases, pressure coefficient increases and the pressure coefficient values are almost the same for all geometries with the increase in rotational speed similar to the previous case.

From Table 2.2 It can be concluded that for both half-million rpm and one million rpm rotating speed of rotor, rotor with three inlets inclined at an angle of 45° is the optimum design compared to the other geometries of the rotor considered after modifying the rotor geometry and for two million and five million rpm rotational speed of the rotor, the rotor with twelve blades is the optimum design of rotor for high-speed spindles compared to the other geometries of the rotor. Rotor geometries considered for numerical simulations of high-speed spindles were the two-stage rotor and its modified geometry. The values of pressure coefficients obtained for different rotational speeds of these rotors are given in Table 2.3. The number of control volumes associated with the numerical simulations of two-stage rotor and its modified geometry were 522,046 and 521,614, respectively. The maximum number of iterations considered for convergence control was 200 and the residual target for convergence criteria was specified as 1e-6 for the geometries. From the table, it could be observed that the pressure coefficient values obtained for the numerical simulations of two-stage rotor and its modified geometry are

Table 2.3 Pressure coefficient values for rotor geometries two-stage rotor and its modified geometry

Geometry	Half-million	One Million	Two Million	Five Million
Two-stage rotor	1.17	1.19	1.20	1.46
Modified geometry of two-stage rotor	1.21	1.26	1.35	1.65

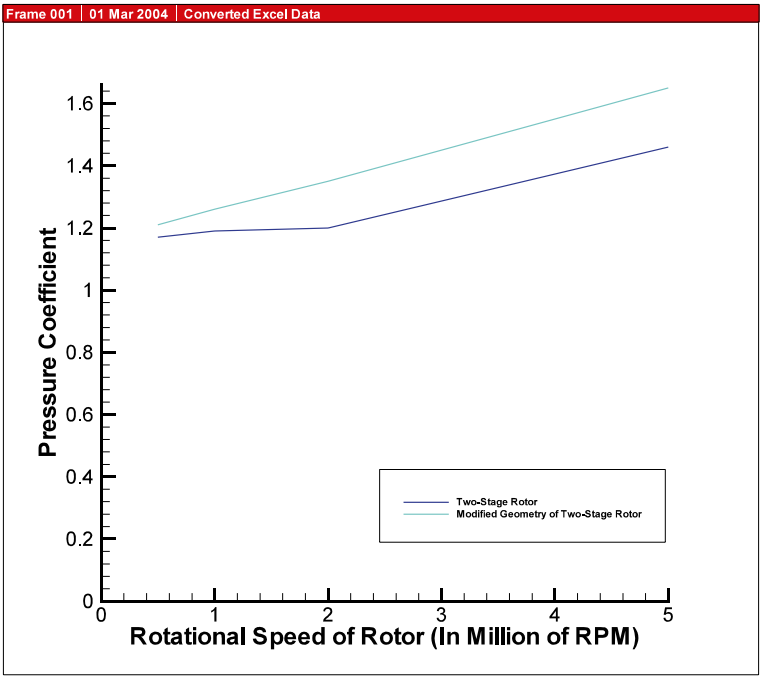

Fig. 2.8 Variation of pressure coefficient with rotational speed for two-stage rotor and its modified geometry. Reproduced with permission. Copyright retained by Inderscience Publishers

very high compared to other geometries of rotor for half-million, one million and two million rpm rotational speeds. The pressure coefficient was found to be almost the same with other geometries of the rotor for five million rpm. Figure 2.8 shows the variation of pressure coefficient with rotational speed of rotor for two-stage rotor and its modified geometry.

From all the geometries discussed above, it can be concluded that for half-million rpm rotational speed of the rotor, rotor with 90° blade angle is the optimum geometry for rotor and for one million rpm rotating speed of the rotor, rotor with three inlets inclined at an angle of 45° is the optimum design compared to other geometries of the rotor. For two million and five million rpm rotational speed of the rotor, rotor with twelve blades is the optimum design of rotor for high-speed spindle compared to the other geometries of the rotor.

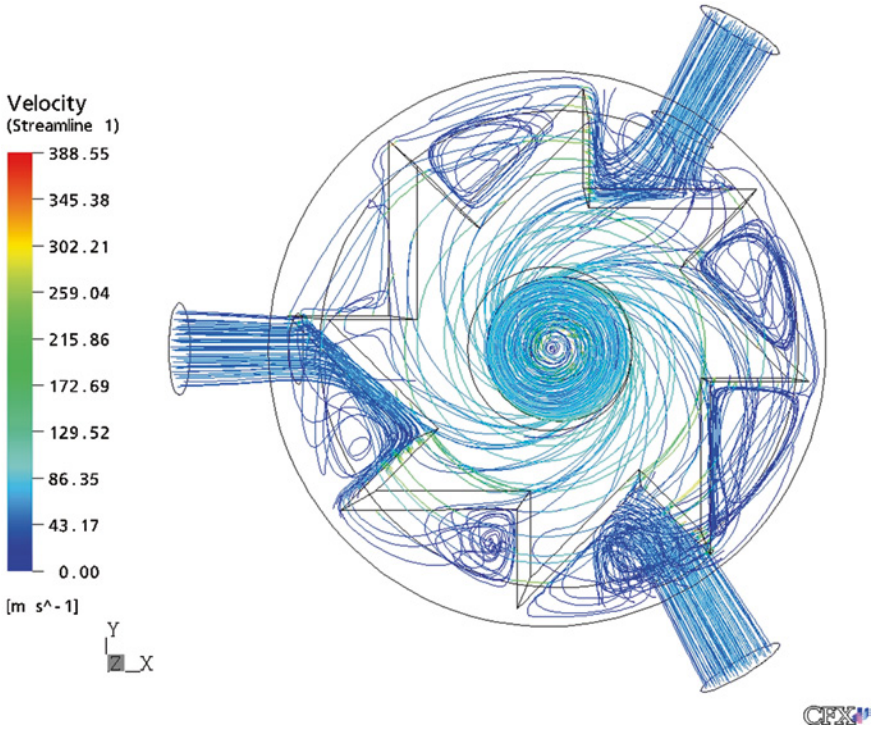

Fig. 2.9 Streamlines describing the flow pattern for rotor with 90° blade angle at one million rpm rotational speed of rotor. Reproduced with permission. Copyright retained by Inderscience Publishers

Flow Topology and Pressure Variations

Flow topology and pressure variation of rotor geometries such as rotor with 90° blade angle, rotor three inlets inclined at an angle of 45°, and two-stage rotor are described.

Rotor with 90° Blade Angle

Flow topology and pressure variation of this geometry will be explained as the pressure coefficient of this geometry was found to be lower than for the other geometries of rotors. The rotational speed of the rotor was specified as one million (1,000,000) RPM.

Flow Topology: Fig. 2.9 shows the flow pattern in rotor with 90° blade angle. Air enters into the housing from three inlets with a pressure of 60 psi and exists from outlet at a pressure of zero. The three inlets are normal to the surface of the housing and the outlet is at the centre of the housing. Air entering from the inlets impinges on the rotor surfaces and flows inside of housing. At the hollow part of the rotor, the fluid is swirled and at the outlet the velocity increases due to the sudden contraction of the surface area at the outlet.

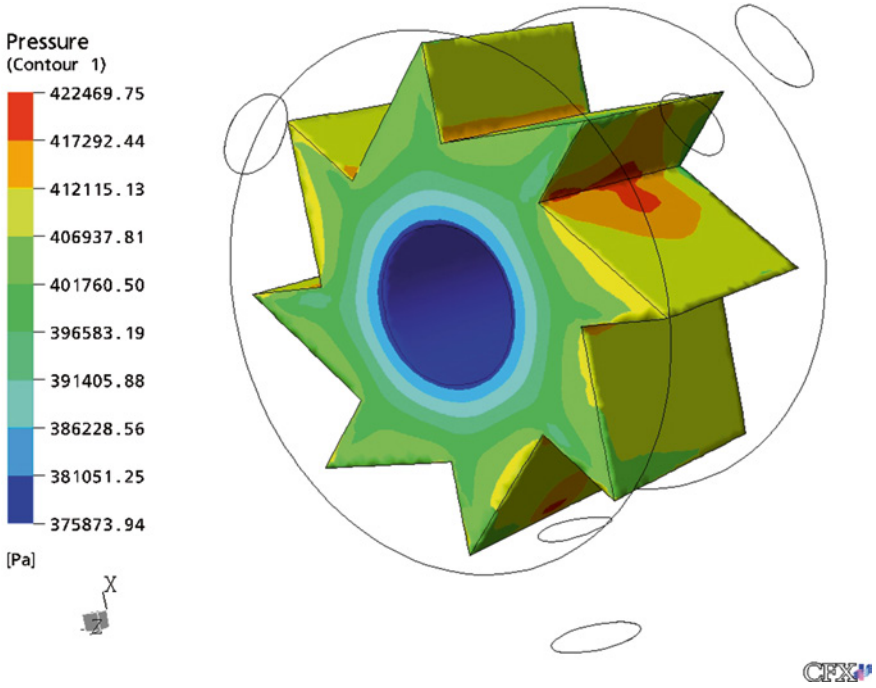

Fig. 2.10 Static pressure distribution on the rotor with 90° blade angle at one million rpm rotational speed of rotor. Reproduced with permission. Copyright retained by Inderscience Publishers

Pressure Variation: Fig. 2.10 describes the pressure variation on the surfaces of the rotor. From the figure it can be observed that the regions of the rotor, where the fluid impinges directly are having maximum pressure due to the stagnation of the fluid compared to the other regions of the rotor. At the stagnation point the total kinetic energy of the fluid is converted into pressure energy, so the maximum pressure occurs at the stagnation point of the fluid. The pressure coefficient on the rotor can be determined from the Eq. 2.9 by substituting values of maximum pressure and minimum pressure on the rotor as shown in Fig. 2.10 and inlet pressure (60 Psi).

Rotor with Three Inlets Inclined at 45°

Flow topology and pressure variation on the rotor with three inlets, inclined at an angle of 45° with z-axis is described. The rotational speed of the rotor was specified as half-million (500,000) rpm.

Flow Pattern: Flow pattern in the geometry can be seen in the Fig. 2.11. Air is entering into the housing from three inlets with a pressure of 60 psi and exists from outlet at a pressure of zero. Fluid entering from three inlets impinges on the rotor blades directly, unlike the previous case (Fig. 2.9), where flow from the inlets is not impinging directly on the rotor blades, but impinging in between the rotor blades. Figure 2.11 clearly shows the impingement of the fluid on the rotor blades. At the hollow part of the rotor, the fluid is swirled and at the outlet the velocity

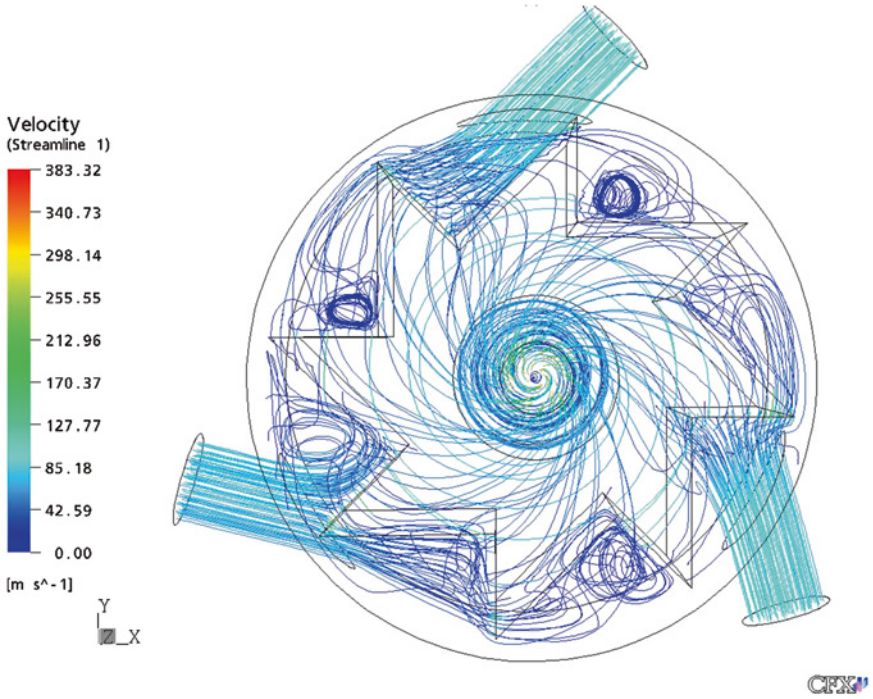

Fig. 2.11 Stream lines describing the flow pattern for rotor with three inclined inlets at an angle of 45° for half-million rpm rotational speed. Reproduced with permission. Copyright retained by Inderscience Publishers

increases due to the sudden contraction of the surface area at the outlet. This forms a vortex flow at the outlet.

Pressure Variation: Fig. 2.12 shows the pressure variation of rotor, along with housing, outlet and three inlets on a plane parallel to X–Y plane, at a distance of 0.08675 inches from the centre, in the z-direction. From the figure it could be seen that the regions of the rotor, where the fluid flow directly impinges are having maximum pressure due to stagnation of fluid when compared to other regions. At the outlet, which is at the centre of the housing pressure is found to be minimum. Figure 2.13 shows the three-dimensional view of the pressure variation on the rotor surfaces. The legend shows the pressure values at different surfaces of the rotor.

Two-Stage Rotor

Flow topology and pressure variation of two-stage rotor is described.

Flow Topology: The inlet static pressure was considered to be 60 psi and outlet static pressure as zero. Rotor's rotational speed was specified as two million rpm (2,000,000). Flow topology is illustrated in Fig. 2.14. Air entering from the upper part of the housing (through inlets 1 and 2) is diverted by rotor blades. One part slides through the upper part of the housing and exits to the atmosphere through outlets 3 and 4, and the other flows over the rotor blade into the housing and exits

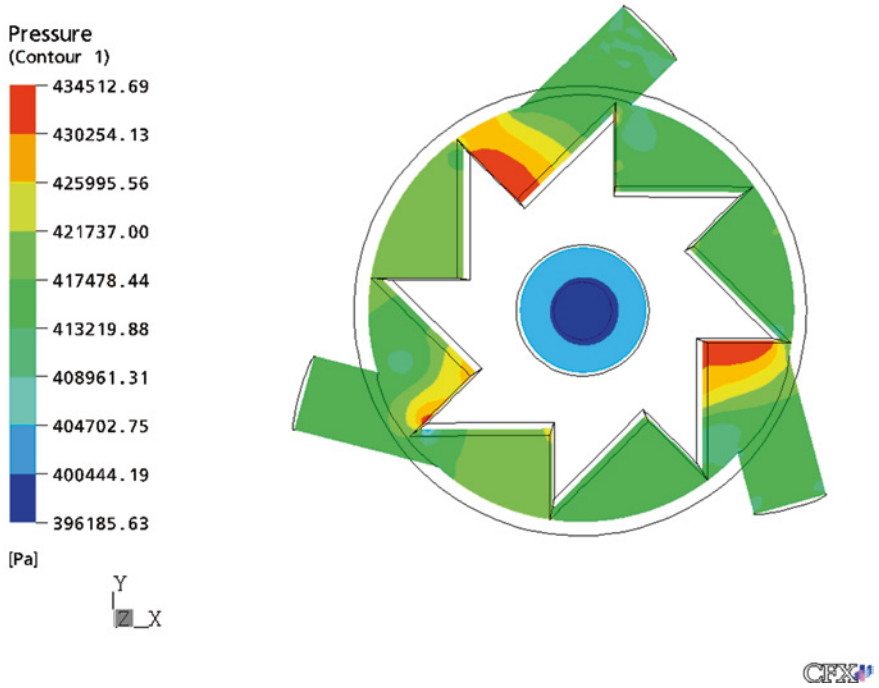

Fig. 2.12 Static pressure variation on the spindle parallel to the X–Y plane for half-million rpm rotational speed. Reproduced with permission. Copyright retained by Inderscience Publishers

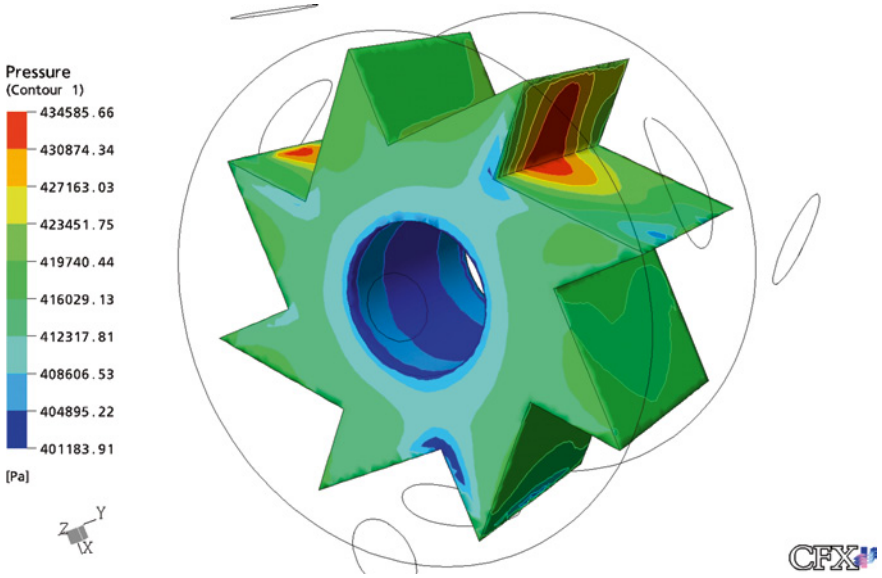

Fig. 2.13 Static pressure distribution on the rotor with three inclined inlets at an angle of 45° for half-million rpm rotational speed of rotor. Reproduced with permission. Copyright retained by Inderscience Publishers

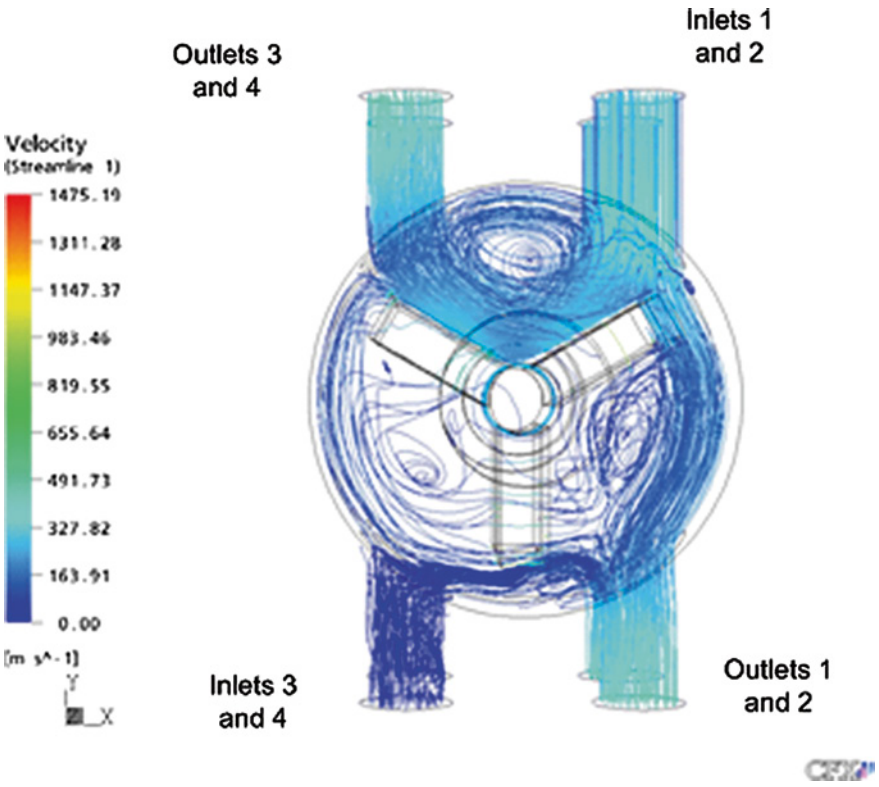

Fig. 2.14 Stream lines describing the flow pattern of two-stage rotor for two million rpm rotational speed of rotor. Reproduced with permission. Copyright retained by Inderscience Publishers

to the atmosphere through the outlets 1 and 2. Fluid entering from the lower part of the housing (through inlets 3 and 4) is bifurcated and most of the fluid builds a re-circulation zone in the lower part of the housing and exits to the atmosphere through outlets 1 and 2 and the other part flows into the housing, and exits to the atmosphere through outlets 3 and 4. From Figs. 2.9, 2.11 and 2.14, it could be observed that the maximum values of velocity of fluid are different, as the rotational speeds of the rotor are different. For rotor with high rotational speed, the maximum velocity is high compared to other rotors.

Pressure Variation: In Fig. 2.15, static pressure distribution of spindle geometry obtained from the numerical simulation of rotor is shown parallel to the X–Y plane at a distance of 3 mm from one side of the rotor (and at a distance of 11 mm from the other side of the rotor) in the z-direction. Air entering from the lower part of the housing impinges directly on the rotor blade surface and the total kinetic energy of the fluid gets converted into the pressure energy due to the stagnation of the fluid. Therefore, the maximum pressure is observed in the vicinity of the leading edge of the rotor blades, which bifurcate the inlet stream entering from the lower part of the housing. Figure 2.16 shows the static pressure distribution on the rotor. The pressure distribution was found to be symmetric on the blades of the rotor.

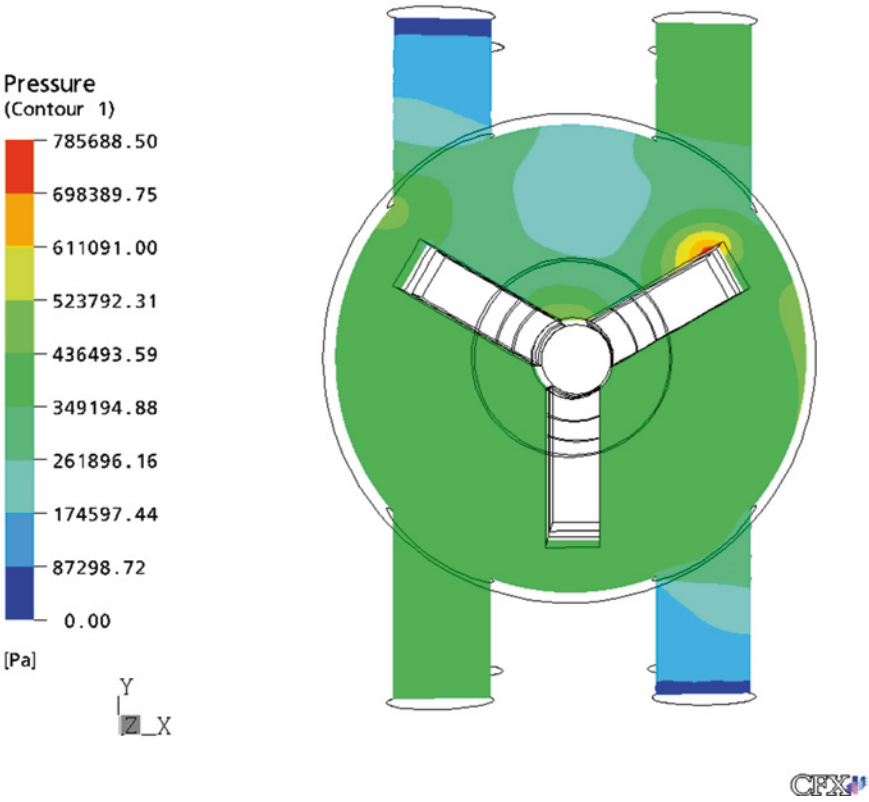

Fig. 2.15 Static pressure contours parallel to X–Y plane for two million rpm rotational speed of rotor. Reproduced with permission. Copyright retained by Inderscience Publishers

Mach Number

Mach number plays an important role for high-speed flows. Mach number on the surfaces of the rotor was found using FLUENT^{TM}. For all the geometries of the rotor at the rotational speeds of half-million rpm, one million and two million rpm, the Mach number is within the subsonic regime, with only a few spots exceeding a Mach number of 1. For rotating speed below two million, the subsonic assumption is well justified. However, for higher rpm, the transonic and supersonic flow regimes need to be taken into consideration.

Using Fluent: Mach number on the surfaces of the rotor was determined using CFD software. FLUENT^{TM} needs the user to specify the flow as subsonic, or supersonic flow as input. Fluent does not require that specification before the calculation. The regime of the flow (subsonic, transonic, or supersonic) comes as part of the solution. The geometry of the rotor with three inlets, inclined at 45° with three inlets and a housing was created and the mesh was created. Volume elements considered for the mesh were approximately 600,000. The ideal gas, air, was considered as the fluid and the k-epsilon

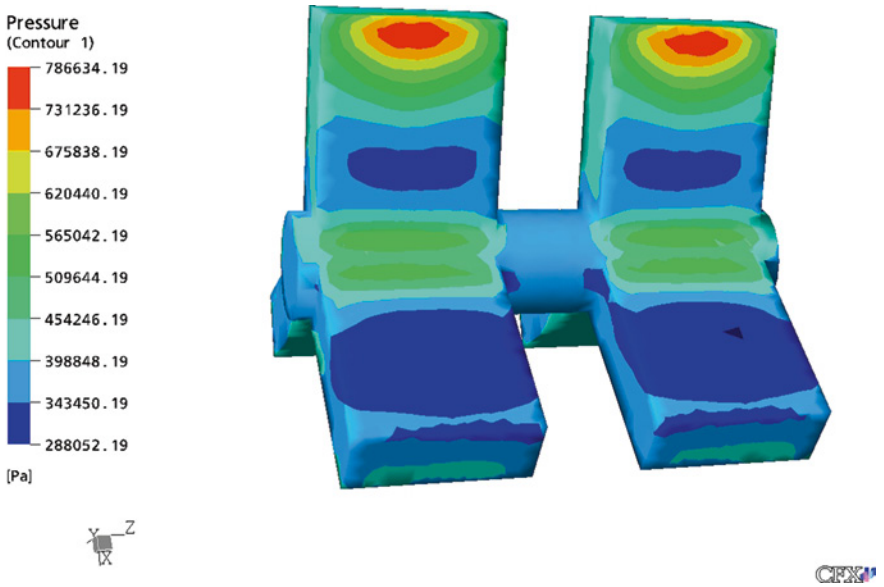

Fig. 2.16 Static pressure distribution on the two-stage rotor for two million rpm rotational speed of rotor. Reproduced with permission. Copyright retained by Inderscience Publishers

turbulence method was used for modelling turbulent flow. An inlet boundary condition, with a pressure of 60 psi was considered at three inlets. At the outlet, outlet boundary condition with a pressure of zero was considered. The rotor was defined as a moving wall with no-slip boundary condition, with an angular speed of two million rpm along its axis. For the remaining surfaces of the geometry, a default no-slip stationary wall boundary condition was applied.

For this compressible flow, a coupled implicit scheme was considered for the solution. The maximum number of iterations for the convergence control for the solver was specified as 4,500 and the target residual for the convergence criterion was specified as 1e-6. The governing equations such as continuity, momentum, energy equations, and equation of state were solved by FLUENT^{TM} and the Mach number at various zones was determined. Figure 2.17 shows the variation of Mach number at three inlets, outlet, and on the rotor surface for the rotational speed of the rotor of two million rpm. From the figure it can be observed that the maximum value of Mach number is 0.96 and the minimum value is 0.01. At the inlets and on the surfaces of the rotor, the Mach number is significantly less than 1 and at the outlet, the value is 0.96. From the results it can be said that only at the outlet, the flow is transonic, as the velocity of the flow is maximum at the outlet because of zero pressure condition. At the inlets and on the rotor surfaces, the flow is found to be subsonic.

An experimental high-speed spindle has been manufactured and is shown in Fig. 2.18. Further experiments are planned that will measure the velocity of the rotor shown in Fig. 2.18 at various inlet air pressures.

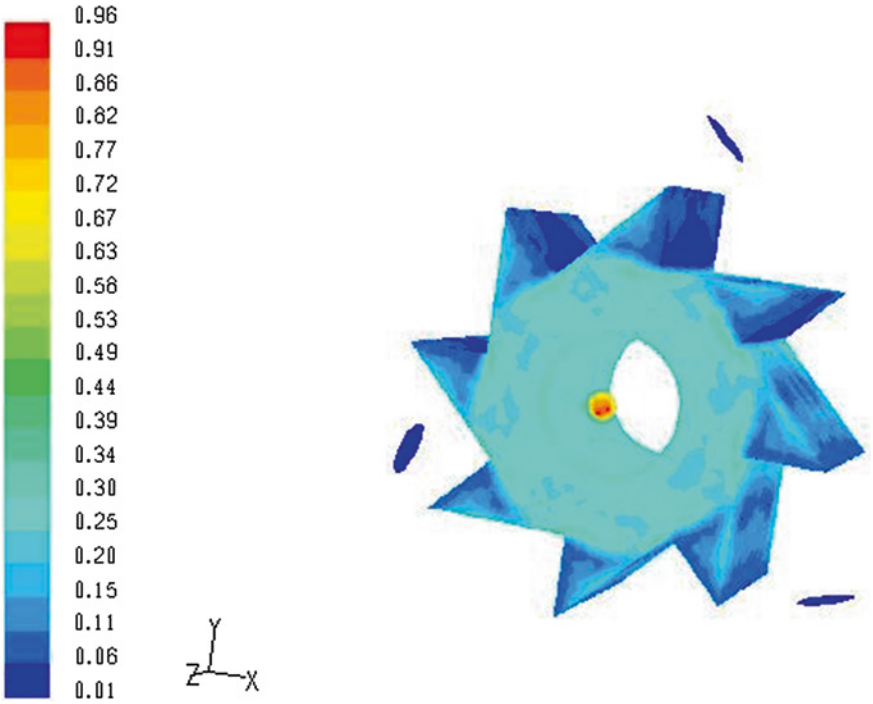

Fig. 2.17 Mach number contours for rotor with three inlets, inclined at an angle of 45° for two million rpm rotational speed of rotor. Reproduced with permission. Copyright retained by Inderscience Publishers

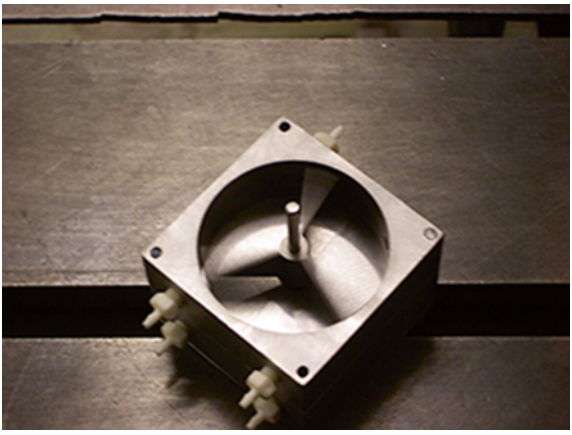

Fig. 2.18 Construction of the prototype three-blade rotor. Reproduced with permission. Copyright retained by Inderscience Publishers

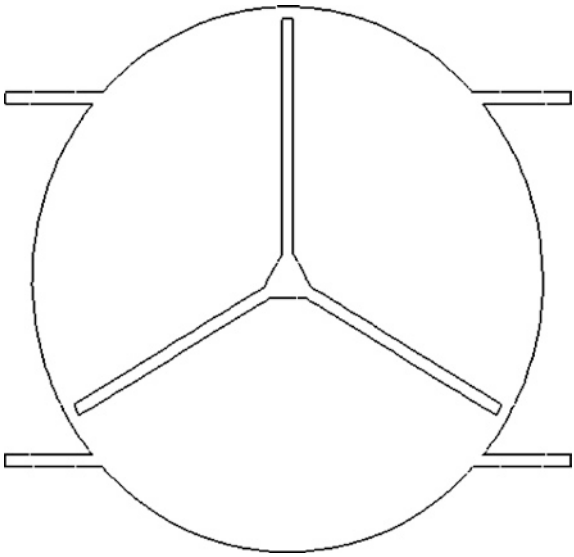

Fig. 2.19 Schematic of the rotor. Reproduced with permission. Copyright retained by Inderscience Publishers

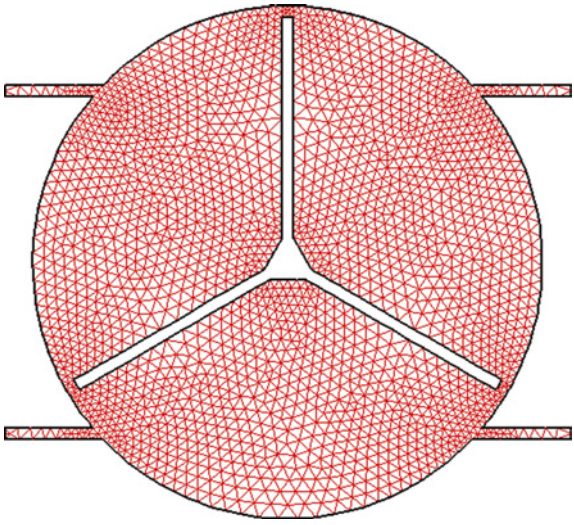

Fig. 2.20 Mesh of the experimental rotor. Reproduced with permission. Copyright retained by Inderscience Publishers

The experimental spindle has been modelled using FLUENT^{TM} to determine the pressures and velocities. The schematic of the spindle is shown in Fig. 2.19.

The grid for this geometry is shown in Fig. 2.20. The grid has been generated in GAMBIT^{TM}. The grid is made of total 2,200 points and triangular mesh elements. The grid is clustered near the tip clearance and near the hub. The inlet to the domain is based on the stagnation pressure and temperature inlet BC while at the outlet the back-pressure of suction is applied. The fluid domain is divided into 2 parts: static fluid and rotating fluid. The static fluid is the fluid portion in the straight ducts of the inlet and outlet where the fluid is not rotating. The rotating

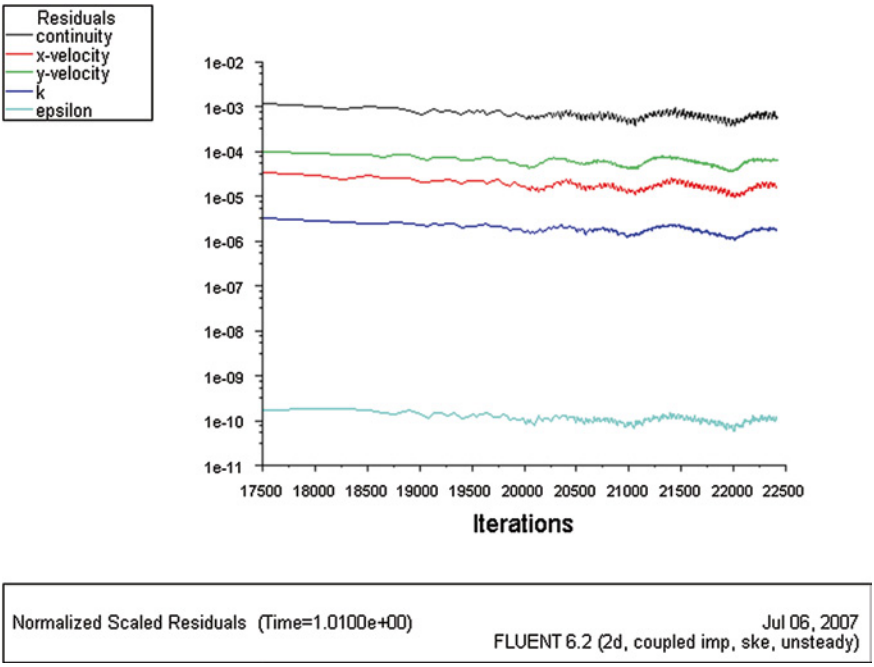

Fig. 2.21 The residual plot of the CFD analysis of the experimental rotor. Reproduced with permission. Copyright retained by Inderscience Publishers

fluid is the fluid surrounding the blades and enclosed in the casing. The angular rotation of half a million rpm is to be applied to the rotating fluid which is explained later.

The residual plot of the rotor is seen in Fig. 2.21, which shows that the solution has not converged. Further analysis is required to produce fully converged results.

The static pressure contours are shown in Fig. 2.22 for the experimental rotor.

The x- and y-velocity contours are shown in Fig. 2.23, whilst Fig. 2.24 shows the total pressure exerted with accompanying flow lines.

The magnitude of velocities and pressure are too high and thus indicates us to re-evaluate our boundary conditions used in the problem. Additional computations can be done with a much denser grid to capture the unsteady dynamics of the problem. Flow topology and pressure variation of different geometries has been described lucidly. Pressure coefficient values of all geometries were given and the variation of pressure coefficient value with the rotating speed of rotor was presented. It can be observed that changes in inlet, outlet, and rotor geometries affect the pressure coefficient significantly in air turbine powered dental hand pieces.

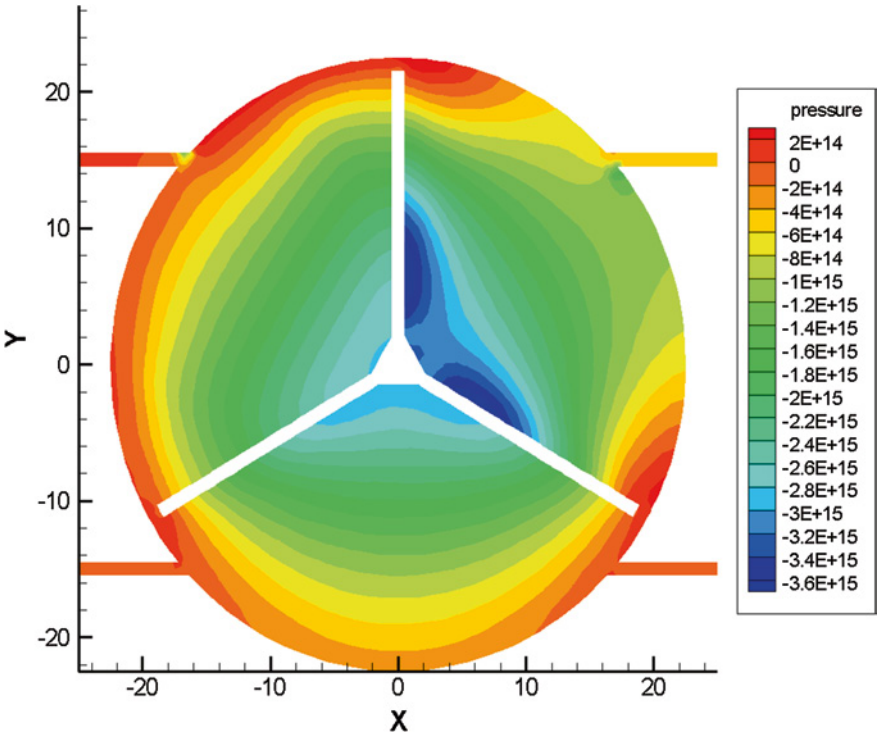

Fig.. 2.22 Static pressure contours of the experimental rotors. Reproduced with permission. Copyright retained by Inderscience Publishers

2.5 Clinical Environment

Conditions in the surgery are different from the laboratory (Silvaggio and Hicks 1997; Borges et al. 1999). The purpose of the coating process is to lengthen the working life of a bur. They will then be available for use on multiple patients, and therefore undergo sterilisation processes. Sterilisation procedures may increase the risk of instrument fracture. It also has the potential to be corrosive and may affect the cutting surface or coating of the bur.

The main sterilisation methods are autoclaves and hot-air sterilisation. The autoclave is the best method of sterilisation for dental instrumentation. The instruments are heated in steam under pressure until conditions are reached which are beyond the survival of any microorganism. Modern autoclaves use electronic programming and monitoring of the condition in the steam chamber in order to ensure that sterilisation is achieved. Hot-air sterilisations are basically simple electric ovens. Hot dry air sterilises effectively but takes much longer than wet heat.

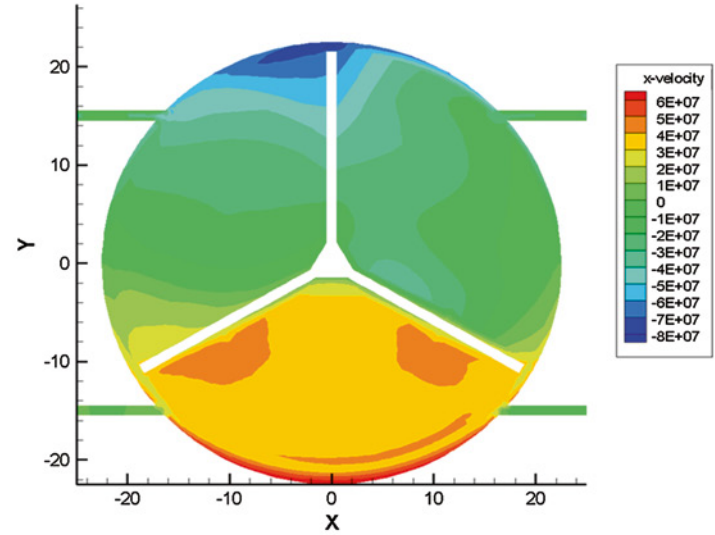

x-velocity contours in m/s

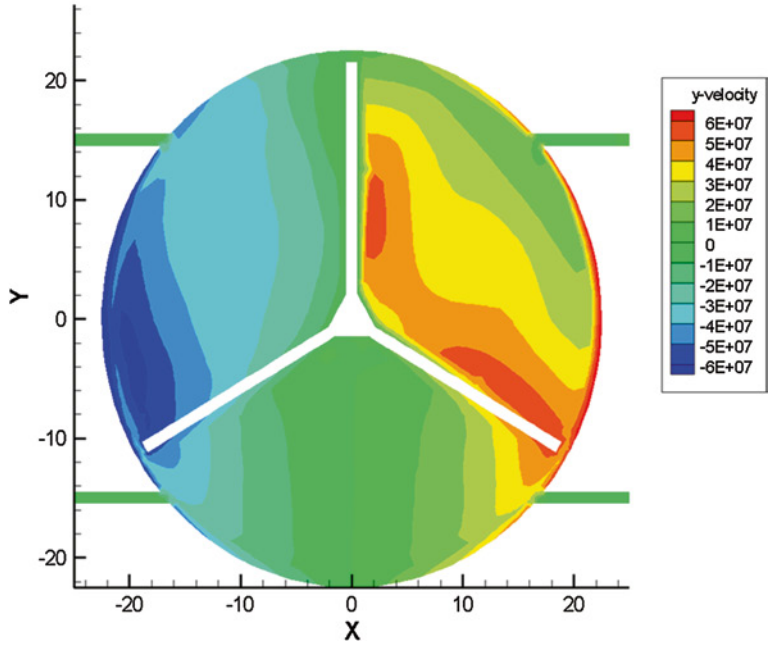

y-velocity contours in m/s

Fig. 2.23 Velocity contours for the experimental rotor. Reproduced with permission. Copyright retained by Inderscience Publishers

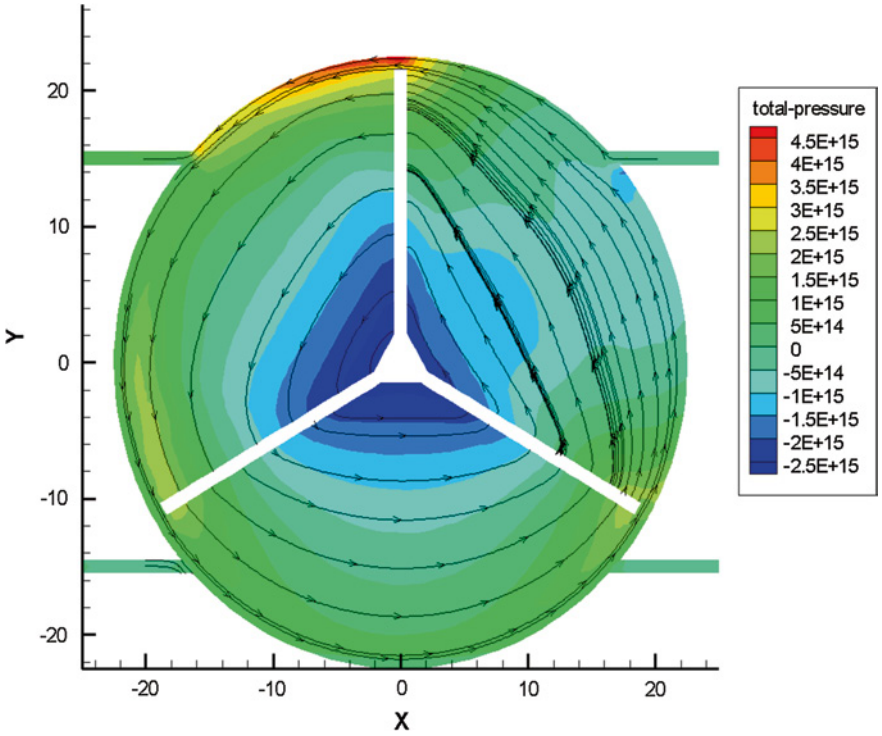

Fig. 2.24 Total pressure in Pa with accompanying flow streamlines for the experimental rotor. Reproduced with permission. Copyright retained by Inderscience Publishers

2.6 Machining Materials with Dental Burs

Wide ranges of tests have been carried out on dental burs. Surprisingly few of these consider the cutting surface and performance of the bur. Many use an approach addressing the physical properties of instrumentation under conditions that are not similar to clinical operating conditions. Those that do simulate clinical conditions tend to be specific with respect to the area of interest and thus the results have very limited relevance outside of the direct application. Also there is no standard covering the testing of burs regarding their performance. The vast majority of the research carried out has used different machine settings, materials methodology and result measurement. This makes it hard to assess the significance of the individual findings and nearly impossible to obtain quantifiable comparison between reports. This research therefore has no fixed guidelines to follow and is entering a field in which there is little background knowledge available.

The most applicable study for this research work is an investigation carried out by Watanabe et al. (2000). They studied cutting performances of air turbine burs on a selection of materials including a range of titanium alloys. They evaluated the

machinability after constant cutting for 5 s. The data was adjusted to account for the density of each metal used. These researchers found for the carbide fissure bur that machinability (**M**) was inversely proportional to the metal hardness (H).

$$M = \frac{k}{H} \tag{2.10}$$

where, k is a empirical constant for the material to be machined.

The diamond points irrespective of the metal used exhibited similar machining efficiencies. It was concluded the differences might be due to the way in which the burs etched. With the use of carbide burs the titanium samples formed accordion-shaped chips. However, when diamond points were used small shapes was formed depending on the size of metal demonstrating the grinding action of the embedded diamond particles.

2.7 Tooth Materials

The mouth is a potentially hazardous environment. The selection of materials for any given application must therefore be considered carefully (McCabe and Walls 2009). Within the oral cavity conditions vary in an irregular manor. For example the variation of temperature in a day may be between 32 and 37 °C depending on whether the mouth is open or closed. The ingestion of hot or cold food or drink however, can extend this temperature range to between 0 and 70 °C. Other important variables include acidity, humidity and tooth impact loading.

2.7.1 Human Tooth

Teeth can be considered as hard, calcified structures. They are attached to the upper and lower jaw, used primarily for chewing food. Each tooth consists of a crown, protruding into the mouth and a root, extending down into the socket as shown in Fig. 2.25, where the junction of the crown and root is the neck of the tooth.

Enamel is the white cap on the crown of the tooth. It is the hardest substance in the body: a calcified material with a very small organic content (less than 4 %). Dentine lines the deep surface of the enamel in the crown, and continues down into the root, surrounding a central pulp cavity. Dentine is like enamel: a calcified matrix, but softer, with some 27 % organic matters, which is mainly collagen. It is believed to house very fine sensory nerve endings.

The dentine is covered on its superficial surface by a layer of cement, yet another calcified tissue going from the neck to the root of the tooth. It has a higher organic content, 50 % by weight. Resembling bone in composition, it is the tissue that receives the collagen fibres of the periodontal membrane, which anchor the tooth to the walls of the socket.

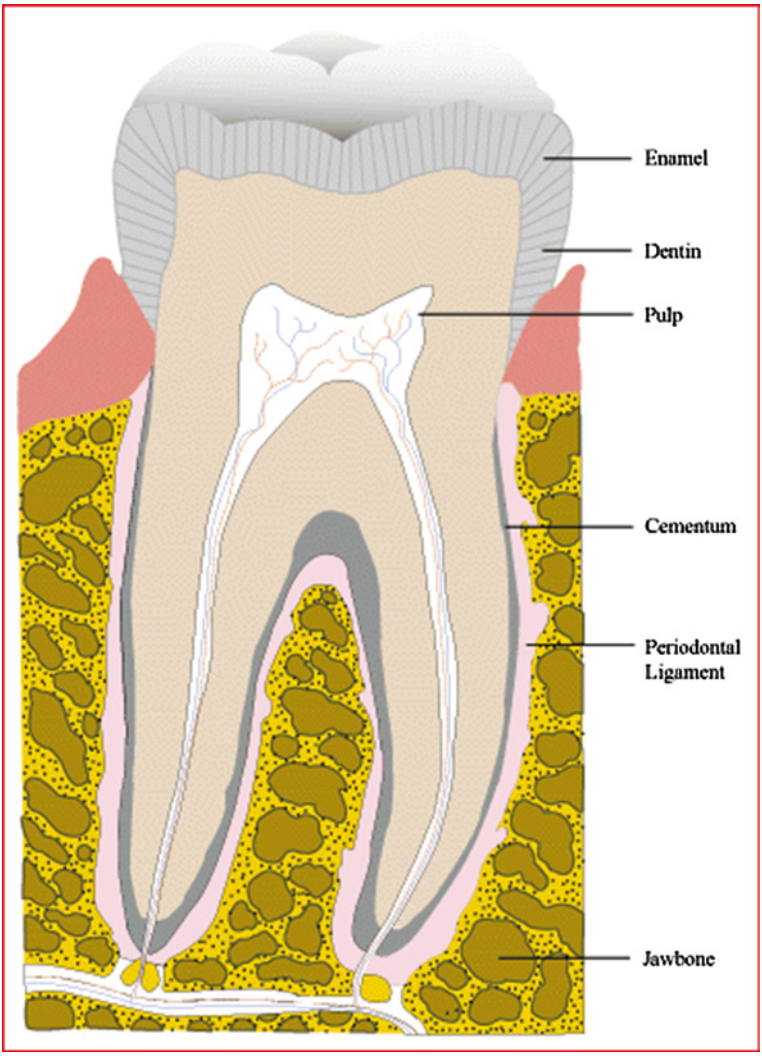

Fig. 2.25 Structure of a human tooth. http://www.vaughns-1-pages.com/local/sunnyvale

2.7.2 Artificial Tooth Materials

Artificial teeth are required to withstand the conditions and loads of normal teeth. The artificial teeth should be strong and tough in order to resist fracture. They should also be hard enough to resist abrasive forces in the mouth and during cleaning, but should allow grinding with a dental bur so adjustments to the occlusion can be made by the dentist at the chair side. The materials most widely used for the manufacture of artificial teeth are acrylic resin and porcelain (McCabe and Walls 2009).

Acrylic resin artificial teeth are produced in reusable moulds by dough or injection moulding. The resins used are highly cross-linked to produce teeth, which are resistant to crazing (when a series of surface cracks have a weakening effect on the whole piece). Acrylic resin has a relatively poor resistance to fatigue fracture and poor impact strength; this makes them more susceptible to abrasion. Acrylic resin is a good thermal insulator.

Porcelain teeth are made in layers. The inner layer is made from a fairly opaque 'core' material. A more translucent 'dentine' material with a translucent 'enamel' porcelain coating forms the outermost layer. Porcelain is a very rigid, hard and brittle material whose strength is reduced by the presence of surface irregularities or internal voids and this can be improved by adding powered alumina to the porcelain.

2.8 Conclusions

In this chapter a brief overview of the dental tools, materials, conditions and operating conditions has been presented. The chapter also describes the oral environment where the dentists work. The size and shape of the dental tool is dictated by where the tool is to be used in the mouth and the amount of material removed. The choice of material is highly dependent on the operating conditions and the environment in which dental bur operates.

When considering high speed dental handpieces, flow topologies and pressure variations of different geometries of air turbine have been described. Pressure coefficient values of all geometries of turbines were given and the variation of pressure coefficient value with the rotating speed of rotor was presented. It can be observed that changes in inlet, outlet, and rotor geometries affect the pressure coefficient significantly. A great deal of research and development is required in the area of high speed dental handpieces.

Acknowledgments The authors are grateful to Inderscience for allowing the authors to reproduce material published in the International Journal of Nano and Biomaterials, 2009, Volume 2, Number 6, p. 505. Inderscience retains copyright of the material used in this chapter. The authors thank their graduate students for contributing to this chapter in helping to formulate the numerical models.

References

Ahmed W et al (2004) Chemical vapour deposition of diamond films onto tungsten carbide dental burs. Tribol Int 37(11–12):957–964

Borges CFM et al (1999) Dental diamond burs made with a new technology. J Prosthet Dent 82(1):73–79

Carvalho CAR et al (2007) The use of CVD diamond burs for ultraconservative cavity preparations: a report of two cases. J Esthetic Restorative Dent 19(1):19–29

Dietz DB et al (2000) Effect of rotational speed on the breakage of nickel-titanium rotary files. J Endod 26(2):68–71

Jian XG et al (2004) Study on the effects of substrate grain size on diamond thin films deposited on tungsten carbide substrates. Key Eng Mater 274:1137–1142
McCabe JF, Walls A (2009) Applied dental materials. Wiley, London
O'Brien WJ (1997) Dental materials and their selection. Quintessence Publication, Chicago
Polini R et al (2004) Cutting force and wear evaluation in peripheral milling by CVD diamond dental tools. Thin Solid Films 469:161–166
Seely RR et al (2007) Essentials of anatomy and physiology. McGraw-Hill, New York
Sein H et al (2003) Stress distribution in diamond films grown on cemented WC–Co dental burs using modified hot-filament CVD. Surf Coat Technol 163:196–202
Sein H et al (2004a) Enhancing nucleation density and adhesion of polycrystalline diamond films deposited by HFCVD using surface treatments on Co cemented tungsten carbide. Diam Relat Mater 13(4–8):610–615
Sein H et al (2004b) Performance and characterisation of CVD diamond coated, sintered diamond and WC–Co cutting tools for dental and micromachining applications. Thin Solid Films 447:455–461
Sein H et al (2002) Application of diamond coatings onto small dental tools. Diam Relat Mater 11(3–6):731–735
Sein H et al (2006) Comparative investigation of smooth polycrystalline diamond films on dental burs by chemical vapor deposition. J Mater Eng Perform 15(2):195–200
Siegel SC, von Fraunhofer JA (1999) Irrigating solution and pressure effects on tooth sectioning with surgical burs. Oral Surg Oral Med Oral Pathol Oral Radiol Endod 87(5):552–556
Silvaggio J, Hicks ML (1997) Effect of heat sterilization on the torsional properties of rotary nickel-titanium endodontic files. J Endod 23(12):731–734
Trava-Airoldi VJ et al (1996a) CVD diamond burs—development and applications. Diam Relat Mater 5(6):857–860
Trava-Airoldi VJ et al (1996b) Development of chemical vapor deposition diamond burs using hot filament. Rev Sci Instrum 67(5):1993–1995
Watanabe I et al (2000) Cutting efficiency of air-turbine burs on cast titanium and dental casting alloys. Dent Mater 16(6):420–425
Yared GM et al (2001) Influence of rotational speed, torque and operator's proficiency on ProFile failures. Int Endod J 34(1):47–53

http://www.springer.com/978-3-319-00647-5

Chemical Vapour Deposition of Diamond for Dental Tools and Burs

Ahmed, W.; Sein, H.; Jackson, M.J.; Rego, C.; Phoenix, D.A.; Elhissi, A.; Crean, S.J.

2014, XI, 140 p. 108 illus., 53 illus. in color., Softcover
ISBN: 978-3-319-00647-5